batteries

MDPI

Article

Thermal Runaway Characteristics of Batteries with Manganese-Based Composite Cathode Materials Triggered by Electromagnetic Induction Heating and Lateral Heating

Changyong Jin [1,2], Shiding Zhou [2], Jing Feng [1], Hongxu Li [1] and Chengshan Xu [1,*]

[1] State Key Laboratory of Intelligent Green Vehicle and Mobility (SKLIGVM), School of Vehicle and Mobility, Tsinghua University, Beijing 100084, China; jinchangyong1@126.com (C.J.)
[2] School of Mechanical Engineering, University of Shanghai for Science and Technology, Shanghai 200093, China
* Correspondence: xcs_pcg@mail.tsinghua.edu.cn

Abstract

Trigger selection underpins thermal runaway (TR) and thermal propagation (TP) testing of lithium-ion batteries, yet its influence on the TR response is rarely quantified, and data for a cell with manganese-based composite cathode (MCC) material are scarce. Here, a fully charged 130 Ah prismatic cell using MCC was driven into TR by high-frequency electromagnetic induction heating and by lateral plate heating in identical fixtures, and each response was resolved into four stages. A 12-s induction pulse initiated TR from a local nucleus: flame ejection followed venting by 9 s, the trigger-point temperature peaked at 682.6 °C, and the voltage collapsed in two stages with a ~3.0-V, ~14-s plateau, the signature of an expanding local short circuit. Lateral heating required 273 s of whole-cell preheating and produced a faster, hotter event: a jet flame ~20 s after venting, whole-cell involvement within 10.4 s, a 775.4 °C peak, and a single-stage ~20-s collapse. Induction heating thus provides rapid, position-selectable initiation with minimal additional energy input, which is well suited to propagation testing, whereas standard-compliant lateral heating represents external-fire abuse; these results provide the first cell-level reference data for MCC thermal runaway, quantify how the triggering method alone alters the TR response, and identify the voltage-collapse morphology as a diagnostic of the initiation mode.

Keywords: lithium-ion battery; manganese-based composite cathode material; thermal runaway; triggering method; electromagnetic induction heating; lateral heating

Check for updates

Academic Editor: Xianglin Li

Received: 18 August 2026
Revised: 10 September 2026
Accepted: 11 September 2026
Published: 12 October 2026

Copyright: © 2026 by the authors. Licensee MDPI, Basel, Switzerland. This article is an open access article distributed under the terms and conditions of the Creative Commons Attribution (CC BY) license.

1. Introduction

After three decades of development, lithium-ion batteries (LIBs) have become the dominant power source for electric vehicles and stationary energy storage [1]. The pursuit of higher energy density, however, is accompanied by growing safety concerns. Under mechanical, electrical, or thermal abuse, a cell may enter thermal runaway (TR), a self-accelerating cascade of exothermic reactions accompanied by rapid temperature rise, gas venting, jet flames, and even explosion [2–4]. For large-format cells the consequences are particularly severe: the two-phase ejecta vented during TR are explosive [5–7], fires can spread multidimensionally in energy-storage configurations [8,9], and the failure behavior depends strongly on both the abuse mode and the cell chemistry [10]. Within a module or pack, the heat released by one failed cell can drive its neighbors into TR, so that a single-cell fault escalates into system-level thermal propagation (TP) [11].

Cathode chemistry largely determines the TR hazard level. High-nickel layered oxides offer high specific energy but exhibit low TR onset temperatures and violent exothermic behavior, whereas olivine-structured lithium iron phosphate (LFP) is thermally milder and currently dominates stationary storage, although large-format LFP systems can still burn and explode under abuse [8,9]. Manganese-based composite cathode (MCC), composed of lithium nickel cobalt manganese oxide (NCM), lithium manganese iron phosphate (LMFP), and lithium manganese oxide (LMO), has recently entered mass production: the higher voltage plateau of the Mn2+/Mn3+ couple raises the energy density by roughly 15–20% relative to LFP [12]. However, the safety performance of such batteries remains unclear. In contrast to the extensive TR literature on NCM and LFP, cell-level TR data for MCC cells remain scarce, and materials-level safety strategies [13–15] cannot substitute for full-cell characterization. Dedicated TR tests on large-format MCC cells are therefore needed to support their safety design and qualification [16].

Thermal propagation testing is now embedded in safety regulations and standards worldwide, including IEC 62619 [17], UL 9540A [18], GB 38031-2020 [19], SAE J2464 [20], and ISO 6469-1 [21], all of which require one cell in the system to be deliberately driven into TR [22]. The validity of such tests hinges on the triggering method, which is expected to initiate TR reliably and reproducibly while introducing minimal additional energy and minimal disturbance to the surrounding cells [23,24]. At the same time, the trigger itself shapes the outcome: the heating power and energy affect the TR and propagation characteristics of the module [16,23], and the same cell can exhibit different TR severities under different triggering methods [25]. How a given chemistry responds to different triggers is therefore both a scientific question and a prerequisite for test standardization.

Commonly used triggering methods each have limitations. Film or plate heaters must heat an entire cell face through the casing, which typically takes hundreds of seconds, preheats the whole cell as well as its neighbors, and adds a considerable amount of external energy before TR begins [23,25]. Nail penetration introduces a mechanical short circuit and breaches the casing, and overcharge alters the electrochemical state of the cell [2,3]. Kriston et al. [26] demonstrated inductive initiation of TR in lithium-ion cells, and electromagnetic induction heating offers an attractive alternative [27–29]: a coil driven by a high-frequency alternating current generates an alternating magnetic field that induces eddy currents in the metallic casing of the cell; owing to the skin effect, the dissipated Joule heat concentrates in a small spot facing the coil, enabling contactless, position-selectable initiation within seconds. Our previous work employed high-frequency induction heating to trigger and visualize TR propagation in battery electrodes in situ [30].

Nevertheless, a direct comparison between induction triggering and the standard-compliant lateral (plate) heating on identical large-format Mn-based cells has not been reported, and how the trigger mode shapes the TR staging, temperature levels, voltage signature, and fire behavior of this emerging chemistry remains unquantified. In this work, we triggered TR in fully charged 130 Ah MCC prismatic cells using (i) high-frequency electromagnetic induction heating and (ii) lateral plate heating, with identical clamping fixtures and instrumentation. Combining synchronized temperature and voltage records with visible and infrared imaging, we resolve the TR process of each mode into four stages, quantify the trigger-dependent differences in triggering time, staging, peak temperatures, and voltage-collapse morphology, and discuss the implications for trigger selection in TR and TP testing of manganese-based batteries.

The contributions of this work are threefold. First, it provides the first cell-level TR characterization of large-format (130 Ah) MCC cells, including the staged temperature–voltage evolution, peak temperatures, venting-to-ignition delays and fire behavior, and places the MCC chemistry between LFP and high-nickel NCM on the basis of a litera-

ture compilation. Second, by applying two triggering methods to identical cells under identical fixtures, it isolates the effect of the trigger itself: the same chemistry exhibits a 93 °C difference in peak temperature, a two-fold difference in venting-to-ignition delay and qualitatively different voltage-collapse morphologies depending only on how TR is initiated, which has direct consequences for the comparability of published TR data and for test standardization. Third, it identifies the two-stage voltage collapse with an intermediate plateau as a signature of TR initiated from a localized nucleus, in contrast to the single-stage collapse of a whole-face onset, providing a simple electrical criterion for diagnosing how a TR event was initiated.

2. Methods and Experiments

2.1. Battery Samples

Large-format manganese-based lithium-ion prismatic cells with an aluminum casing (wall thickness about 0.7 mm), a nominal capacity of 130 Ah and overall dimensions of 300 mm × 150 mm × 30 mm were used in this study. The cathode was a composite manganese-based electrode consisting of NCM, LMFP and LMO (MCC) active materials, Super P carbon black, carbon nanotubes (CNTs), binder and a lithium aluminum titanium phosphate (LATP) solid-electrolyte additive, in a mass ratio of MCC:Super P:CNT:binder:LATP = 94:0.5:1:1.5:3, at a single-side areal loading of 221.3 g/m^2. The anode was graphite-based, consisting of graphite, Super P carbon black, LA133 binder, and SFC (sisal fiber carbon) in a mass ratio of 95:0.5:4.2:0.3, at a single-side loading of 124.4 g/m^2. Each cell contained 450 g of electrolyte. The operating voltage window of the cells is 2.7–4.3 V, with 1.0C charging permitted at temperatures above 0 °C. Prior to the thermal runaway tests, each cell was fully charged to 100% state of charge (SOC; upper cut-off 4.3 V) and then rested at open circuit for more than 10 h before the test; the relaxed open-circuit voltage at the start of the tests was approximately 4.2–4.3 V. Two nominally identical cells were tested, one for each triggering method.

2.2. Thermal Runaway Triggering Methods

The two triggering configurations are illustrated in Figure 1. In both tests the cell was sandwiched in a steel clamping fixture, with mica plates and mica sheets providing thermal and electrical insulation between the cell and the fixture (Figure 1a). The fixtures and clamping conditions were identical for the two methods; only the heat source differed.

For electromagnetic induction triggering, a hairpin induction coil driven by a high-frequency power supply [31] was placed facing the large face of the cell through the fixture window (Figure 1a, left). The alternating magnetic field induces eddy currents in the aluminum casing of the prismatic cell, whose aluminum wall is only about 0.7 mm thick. At the operating frequency the skin depth in aluminum is a few tenths of a millimeter, smaller than the wall thickness, so the eddy currents are confined to the casing wall and the Joule heat is generated primarily in the casing, in a small region facing the coil, from which it is conducted into the adjacent electrode stack (Figure 1b). The local temperature rises rapidly, driving the adjacent anode/separator/cathode stack into a local TR nucleus, which subsequently propagates through the whole cell (Figure 1c). The induction power was applied for 12 s in this study.

For lateral heating triggering, a plate heater (1000 W) covering the large face of the cell was clamped against the cell inside the same fixture (Figure 1a, right). Joule heat generated in the heater conducts through the casing and establishes a through-thickness temperature gradient across the anode/separator/cathode stack (Figure 1d), gradually heating the whole cell toward its TR onset temperature (Figure 1e). The heater was powered continuously until TR initiated, i.e., for 273 s in this test, and was switched off at TR onset.

This configuration corresponds to the external-heating trigger prescribed in current safety standards such as GB 38031-2020 [19].

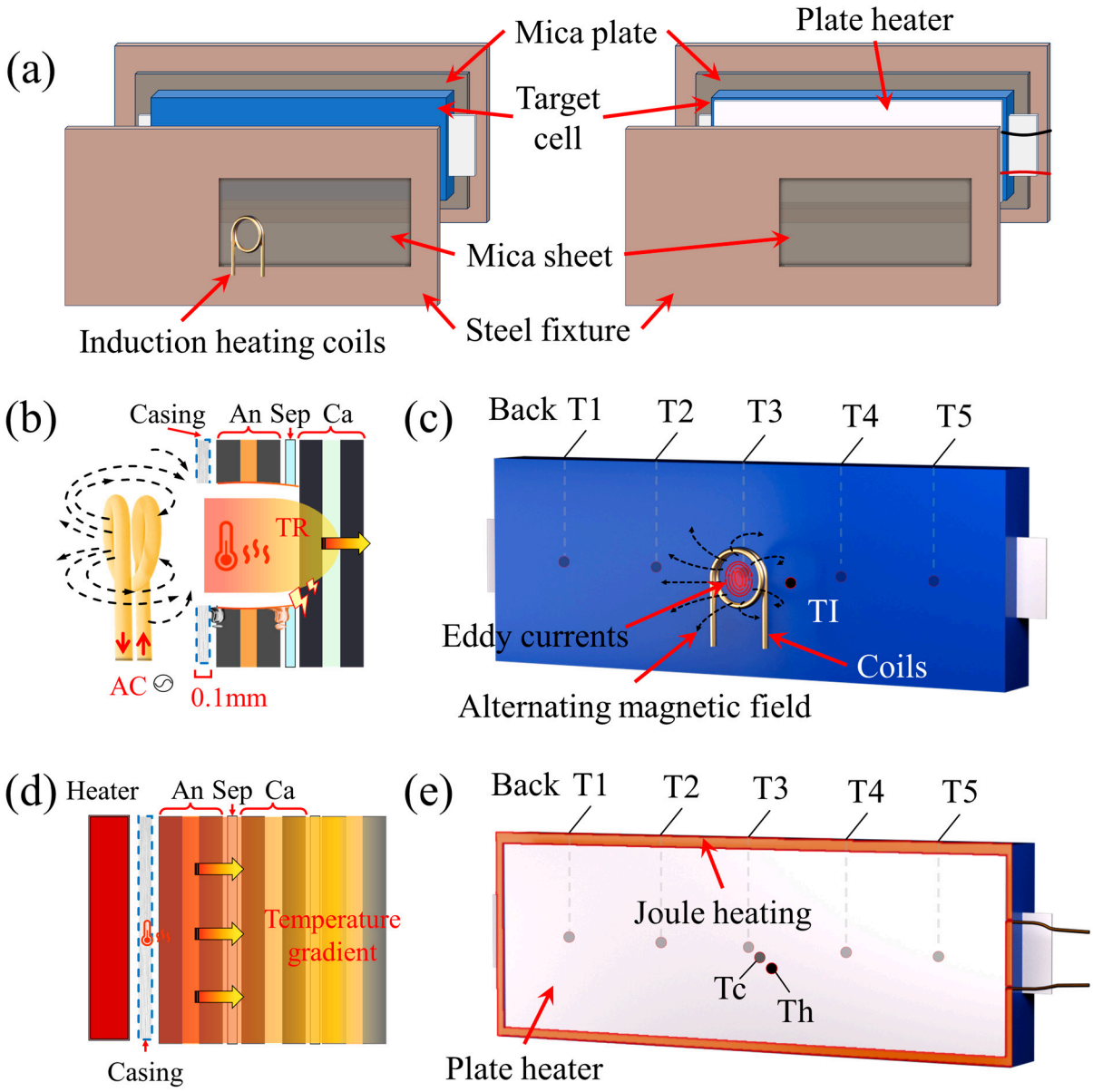


Figure 1. Schematics of the two thermal runaway (TR) triggering methods. (**a**) Exploded views of the clamping fixtures: the target cell is sandwiched between mica plates in a steel fixture; left—electromagnetic induction triggering, with the induction heating coils facing the cell through the fixture window (a mica sheet in between); right—lateral heating triggering, with a plate heater covering one large face of the cell. (**b**) Principle of induction triggering: the high-frequency alternating current (AC) in the coils generates an alternating magnetic field that induces eddy currents in the ~0.7-mm aluminum casing of the prismatic cell, and the Joule heat generated in the casing drives the adjacent anode/separator/cathode (An/Sep/Ca) stack into a local TR nucleus. (**c**) Sensor layout of the induction test: thermocouple TI beside the trigger point and T1–T5 along the centerline of the back face. (**d**) Principle of lateral heating triggering: Joule heat from the plate heater establishes a through-thickness temperature gradient that heats the whole cell toward TR. (**e**) Sensor layout of the lateral heating test: Th on the plate heater, Tc on the cell face adjacent to the heater, and T1–T5 on the back face.

2.3. Instrumentation and Test Procedure

Temperatures were measured with K-type thermocouples (Omega GG-K-30; measuring range up to 1300 °C; accuracy ±1.5 °C or ±0.4%) arranged as shown in Figure 1c,e. In both tests, five thermocouples (T1–T5) were evenly distributed along the centerline of the back face of the cell, i.e., the face opposite to the heat source. In the induction test, an additional thermocouple TI was attached to the front face beside the trigger point; in the lateral heating test, Tc was attached to the front face of the cell adjacent to the heater and Th to the heater surface. The cell terminal voltage was recorded together with all temperature channels at a sampling rate of 10 Hz. The tests were documented by a visible-light video camera and an infrared thermal camera (FLIR T450).

The induction-triggered cell (in its fixture) was tested in the open on a fire blanket, whereas the laterally heated cell was additionally enclosed in a sealed steel box; the influence of this enclosure on the observed fire behavior is noted in the results. The ambient temperature was approximately 30 °C. The tests were carried out at a semi-open test site: the space on the left of the cell and fixture was open to the outdoors, no exhaust extraction was used, and the smoke released during TR drifted outdoors naturally. After mounting and instrumentation, data recording was started, the trigger was applied, and recording continued until the cell had cooled down after TR.

3. Results and Discussion

3.1. Thermal Runaway Characteristics Under Electromagnetic Induction Heating

Figure 2 shows the temperature and voltage records of the induction-triggered test, and Figure 3 the corresponding visible and infrared image sequences; the two figures share the same timeline, in which induction heating starts at 20 s. A single 12-s induction pulse reliably initiated TR: the cell casing ruptured 3 s after the power was switched off, and a jet flame erupted 9 s after that, without any further external energy input. It is worth noting that during the heating window the measured voltage rose anomalously to about 4.36 V (Figure 2b, stage I); this is an electromagnetic-interference artifact of the alternating magnetic field on the voltage measurement leads rather than a real change of the cell voltage, and it disappeared immediately at power-off. Voltage readings taken during an induction pulse should therefore be interpreted with caution.

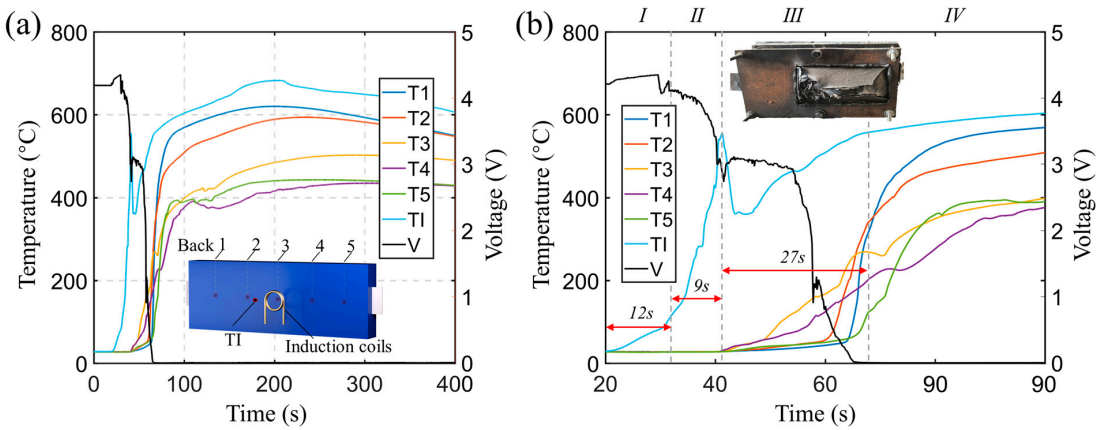


Figure 2. Temperature and voltage responses of the MCC cell triggered by electromagnetic induction heating. (**a**) Overall record: back-face temperatures T1–T5, trigger-point temperature TI, and cell voltage V; the inset shows the thermocouple and induction-coil layout. (**b**) Enlarged view of the TR window, divided into four stages: I—induction heating (12 s); II—venting (9 s); III—jet fire (27 s); IV—decay; the inset shows the cell and fixture after the test. The elevated voltage reading in stage I is an electromagnetic-interference artifact of the induction field on the voltage measurement.

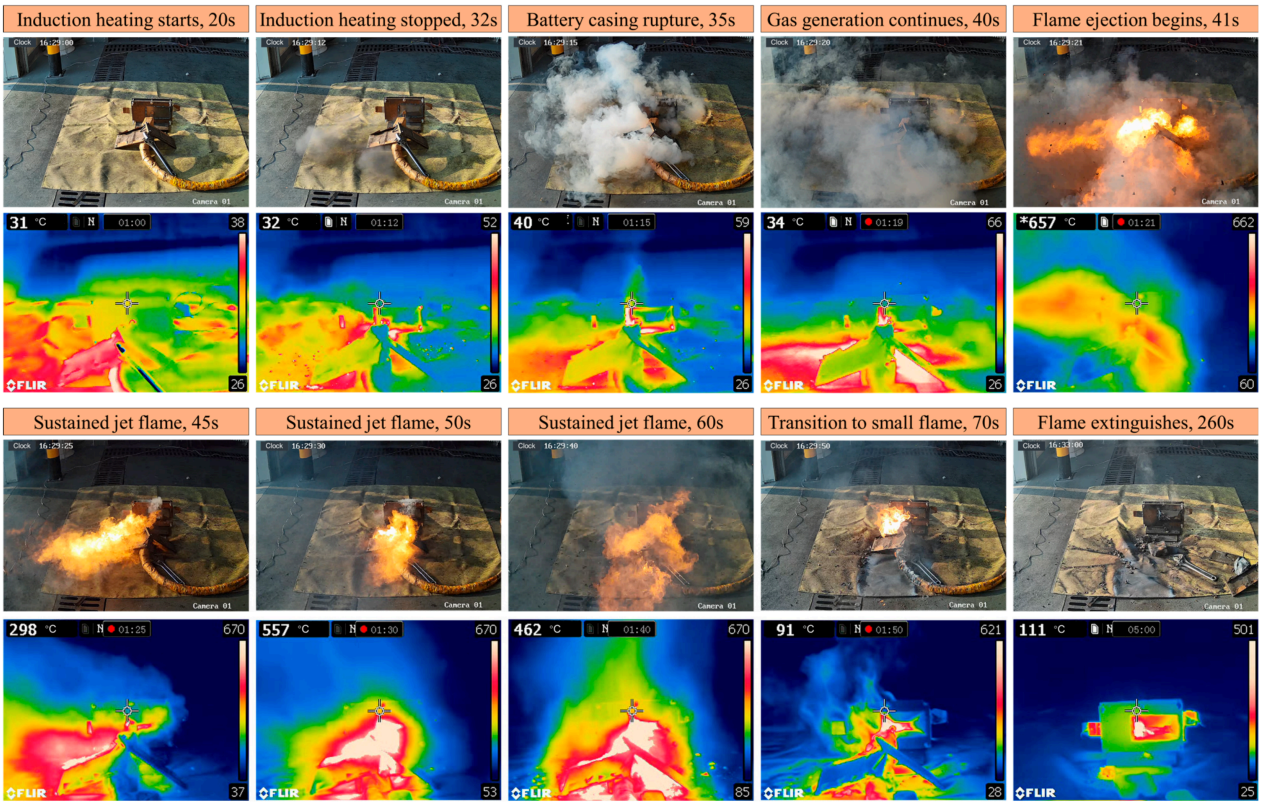


Figure 3. Visible (**upper**) and infrared (**lower**) image sequences of the induction-triggered TR (timeline shared with Figure 2; t = 20 s at the start of induction heating): induction heating starts at t = 20 and stops at 32 s; the battery casing ruptures at 35 s; gas generation continues at 40 s; flame ejection begins at 41 s; the jet flame is sustained during 45–60 s, transitions to small flames at 70 s, and extinguishes at 260 s.

The four stages were delimited by the following criteria, applied identically to both tests. Stage I is the period during which the triggering method is in operation (induction power on, or plate heater on). Stage II begins when TR is identified at the trigger location, i.e., when the temperature-rise rate of the trigger-side thermocouple (TI or Tc) changes abruptly and the cell voltage starts to drop suddenly; venting of the cell accompanies this stage. Stage III is the period during which TR propagates through the interior of the cell, accompanied by the jet fire and by the successive rise of the back-face thermocouples. Stage IV is the period of steady heat transfer after the reactions have ceased, in which all temperatures pass through their maxima and decay.

The TR process can be divided into four stages (Figure 2b). In stage I (induction heating, 12 s, 20–32 s), the trigger-point temperature TI rose from ambient to only about 90 °C at power-off, while the five back-face thermocouples remained essentially at ambient temperature, confirming that the induction energy was deposited locally at the trigger spot. In stage II (venting, 9 s, 32–41 s), the casing ruptured at 35 s (Figure 3), gas generation continued, and TI accelerated sharply as the local TR nucleus formed. In stage III (jet fire, 27 s, 41–68 s), flame ejection began at 41 s, at which moment TI had reached 554.9 °C, and the ejected gases burned as approximately six successive pulsed fireballs (Figure 3, frames at 45–60 s); the infrared camera saturated its 670 °C measurement range during this stage. In stage IV (decay, after 68 s), the jet fire subsided to small flames by 70 s and the flames extinguished at about 260 s; TI reached its maximum of 682.6 °C shortly after the jet-fire stage as heat redistributed through the cell, and the back-face temperatures peaked at 440–620 °C.

The voltage collapse was distinctly two-staged (Figure 2b): the terminal voltage first dropped from about 4.2 V to a plateau of approximately 3.0 V that persisted for about 14 s, and then collapsed to 0 V at a maximum rate of about 4.7 V/s. The plateau indicates that the internal short circuit was initially confined to the triggered zone while the remainder of the electrode stack stayed intact, and the final collapse marks the spread of the short circuit through the whole cell. A plateau at an intermediate voltage rather than at 0 V is expected for a short circuit of finite resistance whose area is small compared with the total electrode area: the cell discharges through the local short while the separator outside the nucleus remains intact, and the terminal voltage settles at a level set by the ratio of the resistance of the intact stack to that of the short. Consistently, the back-face thermocouples responded sequentially outward from the trigger location: T3 and T4, which face the coil position, started rising first, followed by T2, then T1, and finally T5, spanning roughly 25 s in total. Both the staged voltage collapse and the sequential thermocouple response demonstrate that induction triggering produces a point-like TR nucleus that propagates across the cell, rather than a simultaneous whole-cell event.

3.2. Thermal Runaway Characteristics Under Lateral Heating

Figure 4 shows the temperature and voltage records of the lateral heating test, and Figure 5 the corresponding visible and infrared sequences (in Figures 4 and 5, t = 0 is the start of data recording and heating starts at t = 20 s). In contrast to the 12-s induction pulse, the plate heater was powered from t = 20 s to t = 293 s, for 273 s, before TR initiated. During this preheating stage (stage I in Figure 4b), the heater temperature Th rose steadily to about 360–370 °C, the adjacent cell face Tc followed to about 315 °C at TR onset, and the back face of the cell reached up to about 90 °C; the whole cell was thus substantially preheated before TR began. The heater was switched off at TR initiation, and the subsequent TR evolved without further external energy input.

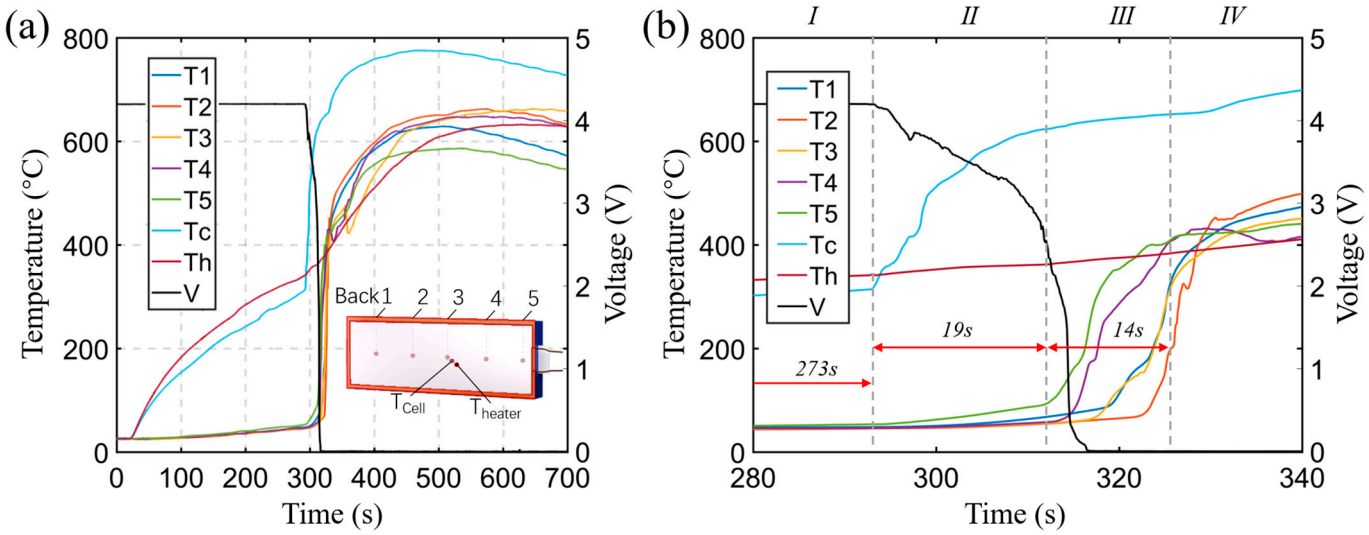


Figure 4. Temperature and voltage responses of the MCC cell triggered by lateral heating. (**a**) Overall record: back-face temperatures T1–T5, cell-face temperature Tc, heater temperature Th, and cell voltage V; the inset shows the thermocouple layout. (**b**) Enlarged view of the TR window, divided into four stages: I—lateral preheating (heating from t = 20 s to t = 293 s, i.e., 273 s); II—venting (19 s); III—jet fire (14 s); IV—decay.

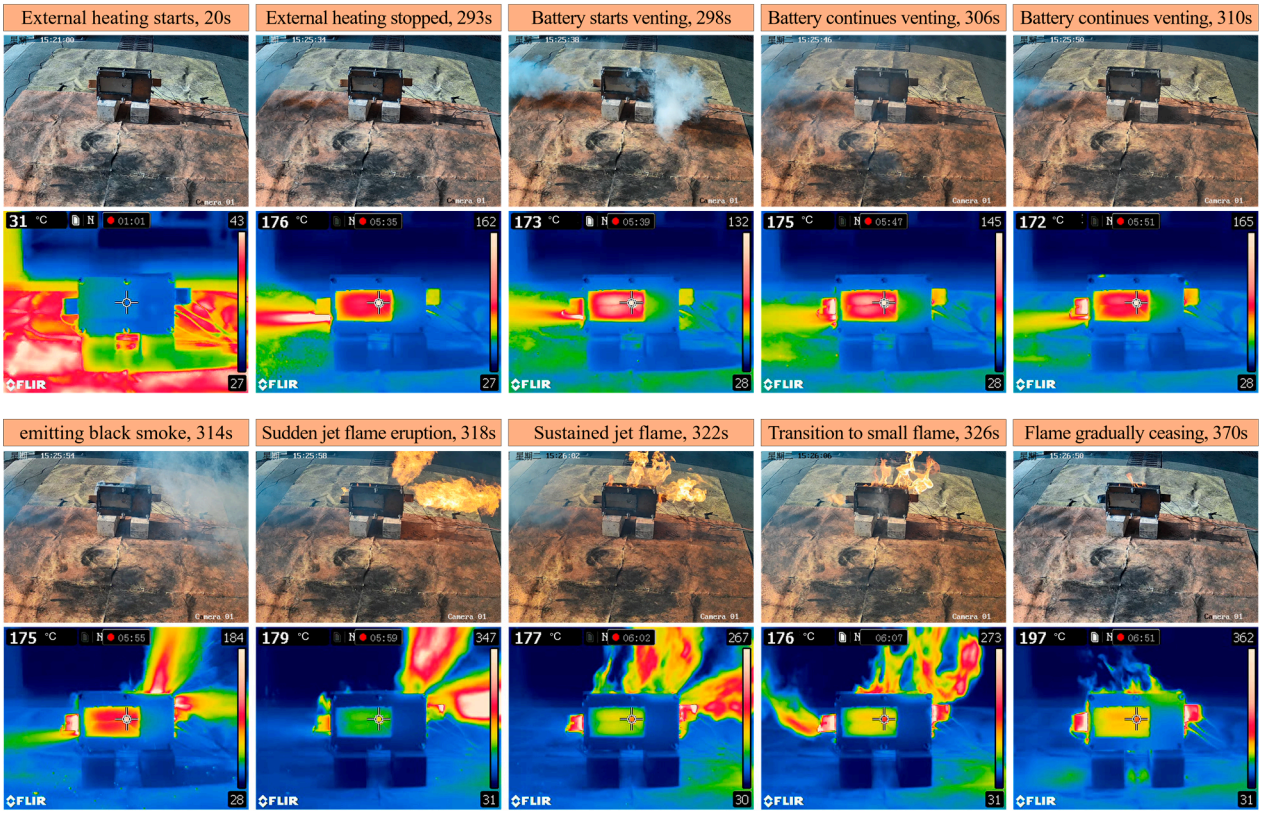


Figure 5. Visible (**upper**) and infrared (**lower**) image sequences of the lateral-heating-triggered TR (times counted from the start of data recording): external heating starts at 20 s and stops at 293 s; the cell starts venting at 298 s and continues venting during 306–310 s; black smoke is emitted at 314 s; a jet flame suddenly erupts at 318 s and is sustained at 322 s; the flame transitions to small flames at 326 s and gradually ceases by 370 s.

The subsequent evolution again falls into four stages (Figure 4b), delimited by the same criteria as in Section 3.1. In stage II (venting, 19 s), Tc surged from about 315 °C to above 600 °C as TR nucleated at the heated face; the cell started venting white smoke at 298 s and continued venting through 306–310 s, turning to black smoke at 314 s (Figure 5). The terminal voltage began to decline at the same time and fell monotonically, in a single stage without any plateau, reaching 0 V about 20 s after the onset of decline. The absence of a plateau is attributed to the state of the heated face, which had already reached about 315 °C, far above the shutdown and melting range of the separator, so that the separator failed over a large area at once. In stage III (jet fire, 14 s), a sudden jet flame erupted at 318 s (Figure 5, 318 s frame), and all five back-face thermocouples surged in rapid succession—in the order T5, T4, T3, T1, T2—within a window of only 10.4 s, with local heating rates up to about 142 °C/s, indicating that the reaction swept through the entire cell almost simultaneously. In stage IV (decay), the jet flame subsided to small flames within about 8 s (Figure 5, 326 s) and the flames gradually ceased by about 370 s. The cell-face temperature Tc continued to rise after the flames subsided and peaked at 775.4 °C, the back-face temperatures peaked at 586–663 °C, and the heater, in turn heated by the cell, reached about 630 °C.

Because the laterally heated cell was enclosed in a sealed steel box, the fire behavior outside the box was strongly attenuated: open flames above the box persisted for only about 50 s, and the outer wall of the box stayed below about 310 °C throughout the test. The enclosure limits the oxygen supply and shields the jet, so the external fire appears milder than in the open induction test even though the internal TR was more severe in all

measured temperatures. This difference in boundary conditions should be kept in mind when comparing the flame behavior of the two tests.

3.3. Comparison of the Two Triggering Methods

Table 1 summarizes the comparison. The most direct difference lies in the triggering duration and its effect on the initial cell state: induction heating initiated TR with a single 12-s localized pulse, leaving the bulk of the cell at ambient temperature at TR onset, whereas lateral heating required 273 s—more than twenty times longer—and preheated the entire cell (front face about 315 °C, back face up to about 90 °C) before TR began. For thermal propagation testing this difference has two consequences: the long preheating of a plate heater inevitably transfers heat to neighboring cells and thermal barriers, altering the initial conditions of the propagation process that the test is intended to characterize, whereas the localized induction pulse leaves the surroundings essentially undisturbed [16,23,26].

Table 1. Comparison of the thermal runaway triggering characteristics of the two methods on the MCC cells.

Item	Electromagnetic Induction Heating	Lateral Heating
Heating duration until TR initiation	12 s	273 s
Heated region	Local spot on the casing facing the coil	Entire large face of the cell
Cell state at TR onset	Bulk near ambient; TI about 90 °C at power-off	Whole cell preheated; Tc about 315 °C, back face up to about 90 °C
Venting behavior	Casing rupture 3 s after power-off	White smoke to black smoke over about 20 s
Venting to flame ejection	9 s	About 20 s
Jet-fire stage	27 s, about 6 pulsed fireballs	14 s, single sustained jet
Peak temperature (hottest TC)	682.6 °C (TI, trigger point)	775.4 °C (Tc, heated face)
Back-face peak temperatures	440–620 °C	586–663 °C
Back-face onset spread	About 25 s, sequential (T3/T4, then T2, T1, T5)	10.4 s, near-simultaneous (T5, T4, T3, T1, T2)
Voltage collapse	Two-stage; plateau at about 3.0 V for about 14 s	Single-stage; about 20 s to 0 V
Test enclosure	Open fixture on a fire blanket	Fixture in a sealed steel box (outer wall below about 310 °C)

Both methods produced a four-stage TR process (triggering/preheating, venting, jet fire, and decay), but the staging and severity differed systematically. The induction-triggered cell vented 3 s after power-off and ignited 9 s later, then released its energy as about six pulsed fireballs over a 27-s jet-fire stage; its hottest measured temperature was 682.6 °C at the trigger point, and the back-face onsets spread sequentially over roughly 25 s—the signature of a TR front propagating from a point nucleus. The laterally heated cell, once triggered, developed faster and reached higher temperatures: venting was followed by a jet flame within about 20 s, the whole cell became involved within 10.4 s, and the peak temperatures were higher both at the heated face (775.4 °C) and on the back face (586–663 °C). The higher severity is consistent with the substantial thermal energy stored in the cell during the 273-s preheat, which brings the entire electrode stack close to its reaction onset so that TR, once nucleated, involves the entire cell almost simultaneously; the sealed enclosure may additionally have reduced convective heat losses. These peak temperatures

are compared with literature data for NCM/NMC and LFP cells in Section 3.4, where the resulting positioning of the MCC chemistry is discussed.

The terminal voltage clearly reflects the triggering mode: a two-stage collapse with a ~3.0-V, ~14-s plateau under induction (a local short circuit that subsequently spreads) versus a single-stage ~20-s collapse under lateral heating (a whole-face onset). The voltage trace alone can thus indicate how localized the initiating fault was, which is a useful diagnostic for post-test analysis and field failure investigation. Regarding method selection: electromagnetic induction heating provides rapid, contactless, position-selectable initiation with minimal additional energy input, making it well suited to system-level thermal propagation tests in which the initial conditions of neighboring cells must remain undisturbed; its main caveats are the electromagnetic interference on voltage measurements during the pulse and the fact that it has not yet been included in test standards. Lateral plate heating conforms to existing standards such as GB 38031-2020 [19] and emulates the practically relevant scenario of a cell heated by an external fire or a failed neighbor, at the cost of long preheating, high added energy, and a modified initial cell state. The two methods are therefore complementary: induction heating for propagation-oriented testing, and lateral heating for standard-compliant, worst-case severity assessment of manganese-based batteries.

3.4. Discussion

The two tests demonstrate that the triggering method strongly affects the TR response: it determines the initial thermal state of the cell and thereby shapes the entire TR event. Induction heating delivered its energy to a spot on the casing within 12 s, so TR started from a localized nucleus in an otherwise cold cell and had to propagate across the electrode stack, which is reflected in the sequential back-face temperature onsets spanning roughly 25 s and in the two-stage voltage collapse. Lateral heating, by contrast, heated the whole cell toward its reaction onset over 273 s, so that once TR nucleated, the remaining material followed within about 10 s, producing a hotter and more synchronized event. Reported TR characteristics of nominally identical cells therefore depend on the trigger, and cross-study comparisons of peak temperatures or venting-to-ignition delays [16,23,25] should always be interpreted together with the triggering conditions.

The results position the TR hazard of the MCC chemistry between the two established cathode families, as summarized in Figure 6, which compiles reported peak cell-surface temperatures under lateral heating triggering together with the present measurements. At full charge, large-format high-nickel layered-oxide cells reach the highest temperatures—in particular, a 75 Ah NCM811 pouch cell tested by the same group averaged about 1018 °C [32]—and NCM/NCA cells of other formats cluster at about 690–800 °C [33–36]. Fully charged large-format LFP cells, by contrast, peak at only 581–594 °C [37,38], and lower states of charge reduce the peak temperatures further in every family. The present Mn-based cells fall between the two families: 682.6 °C under induction triggering and 775.4 °C under lateral heating—roughly 240–340 °C below the NCM811 benchmark, yet about 100–180 °C above the large-format LFP level, and, unlike the LFP cells, above the melting point of aluminum (660 °C), a threshold relevant to the integrity of aluminum casings and busbars. The incorporation of NCM and LMO into the composite cathode raises the energy density but carries a measurable thermal penalty relative to LFP, while the phosphate component still provides a substantial margin relative to high-nickel chemistries.

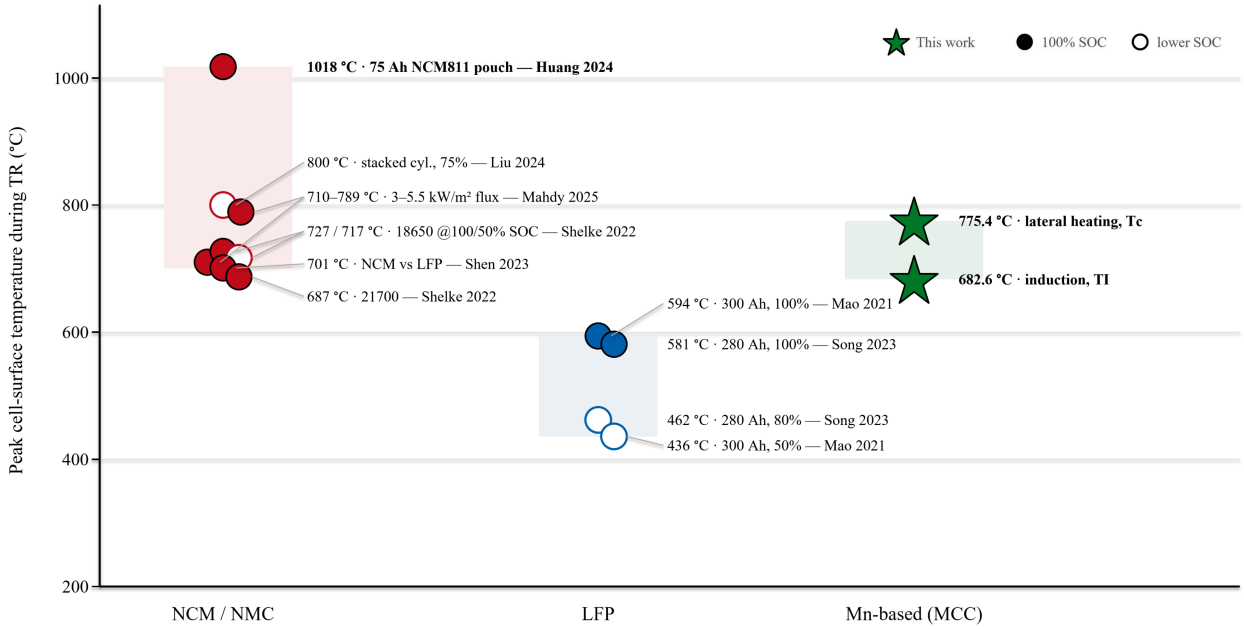


Figure 6. Peak cell-surface temperatures during TR under lateral heating triggering: literature data for NCM/NMC and LFP cells compared with the present Mn-based (MCC) results. Each point is annotated with the peak temperature, the cell format and SOC, and the source (first author and year). Green stars—this work (130 Ah MCC prismatic cells, 100% SOC); filled circles—100% SOC (or SOC unspecified); open circles—lower SOC; shaded bands—the span of each chemistry family. The 75 Ah NCM811 pouch cell [32] was tested by the same group and provides the closest large-format benchmark (about 1018 °C versus 682.6–775.4 °C). Literature sources: Huang et al. 2024 [32]; Shelke et al. 2022 [33]; Liu et al. 2024 [34]; Mahdy et al. 2025 [35]; Shen et al. 2023 [36]; Song et al. 2023 [37]; Mao et al. 2021 [38].

The comparison in Figure 6 is necessarily indicative rather than exact, because the compiled cells differ in capacity (from 18650/21700 cells of a few ampere-hours to 280–300 Ah prismatic cells), format, venting design, test enclosure, and thermocouple location, all of which influence the measured peak surface temperature independently of the cathode chemistry. Larger cells generally reach higher peak temperatures because their thermal mass grows faster than their heat-dissipating surface, and enclosed tests retain more heat than open ones. These effects, however, act against rather than in favor of the ordering inferred here: the 130 Ah MCC cells peaked 240–340 °C below a smaller (75 Ah) NCM811 cell tested by the same group and 100–180 °C above much larger (280–300 Ah) LFP cells, so the ordering NCM $\geq$ MCC > LFP is unlikely to be an artifact of cell size. The absolute differences should nevertheless not be read as chemistry-only values, and the same-group NCM811 benchmark carries the most weight.

More importantly, both tests ended in violent jet fires with multi-second flame ejection: the composite cathode moderates, but does not eliminate, the fire hazard of a fully charged large-format cell. The venting-to-ignition delays of 9 s (induction) and about 20 s (lateral heating) constitute a short but usable window for early warning and suppression measures at the system level [13–15].

The electrical and thermal signatures carry mechanistic information beyond the tests themselves. The two-stage voltage collapse under induction—a ~3.0-V plateau sustained for ~14 s before the final drop—indicates an internal short circuit initially confined to the triggered zone, whereas the single-stage ~20-s collapse under lateral heating indicates a whole-face onset; the voltage trace alone thus reveals the locality of the initiating fault. The back-face onset spread (about 25 s versus 10.4 s) provides a complementary thermal measure of in-cell propagation. Both signatures are consistent with our earlier in-situ

imaging of induction-triggered electrodes, in which the reaction front nucleates at the heated spot and then sweeps across the electrode plane [30]. Such signatures could also be useful in post-incident analysis: the shape of the recorded voltage collapse may help distinguish a localized internal fault from bulk external heating.

Several limitations of this study should be noted. Each cell-level triggering mode was tested on one cell; although the four-stage structure and the key timings are mutually consistent across the temperature, voltage, and imaging records, replicate tests are needed to establish reproducibility [24]. In addition, the tests were limited to 100% SOC, the surface thermocouples underestimate the internal temperatures, the gas composition and mass loss were not measured, and the cells have a specific composite-cathode design with an LATP additive, so the results may not transfer directly to MCC cells of other designs. The enclosures differed—the induction test was run in an open fixture while the laterally heated cell was enclosed in a sealed steel box—which mainly affects the visible fire behavior and convective losses rather than the triggering itself; tests with matched enclosures would make the severity comparison more rigorous. The energy delivered by each trigger was not metered, and the induction pulse distorts the voltage reading during heating, so future work should add power metering and a short measurement blanking window.

Future work will therefore (i) repeat both tests under matched enclosures with at least three cells per method to establish reproducibility; (ii) meter the triggering energy so that the parasitic energy input of each method can be compared quantitatively; (iii) extend the tests to lower states of charge and to MCC cells of other capacities, formats and designs, which will also clarify the influence of cell capacity and format on the peak temperature; (iv) add gas analysis and mass-loss measurements; and (v) apply the induction trigger in module- and system-level thermal propagation tests, where its rapid, low-energy initiation leaves neighboring cells undisturbed [16–23,26]. Combining such tests with in-situ observation of the reaction front [30] would allow the relation between the initiation mode, the front propagation speed and the voltage-collapse morphology to be established quantitatively.

4. Conclusions

This study compared two methods of triggering thermal runaway in fully charged 130 Ah manganese-based composite cathode (MCC) prismatic cells—high-frequency electromagnetic induction heating and lateral plate heating—under identical clamping fixtures and instrumentation, and resolved each event into four stages (triggering/preheating, venting, jet fire, and decay) using synchronized temperature/voltage records together with visible and infrared imaging. The main conclusions are as follows.

First, both methods triggered TR reliably in a single attempt, but with markedly different characteristics. Induction heating initiated TR with a 12-s localized pulse that left the bulk of the cell at ambient temperature: the casing ruptured 3 s after power-off, flames ejected 9 s later, about six pulsed fireballs developed over a 27-s jet-fire stage, the trigger-point temperature peaked at 682.6 °C, and the voltage collapsed in two stages with a ~3.0-V plateau lasting ~14 s. Lateral heating required 273 s of whole-face preheating, with the heated cell face at about 315 °C at TR onset: venting was followed by a sudden jet flame within about 20 s, all five back-face thermocouples surged within 10.4 s, the hottest temperature reached 775.4 °C, and the voltage collapsed in a single ~20-s stage.

Second, the trigger mode governs the locality of TR initiation and can be identified directly from the measured signals: a point-like nucleus with sequential in-cell propagation and a two-stage voltage collapse under induction, versus near-simultaneous whole-cell involvement with a single-stage collapse after bulk preheating. For test practice the two methods are complementary. Induction heating provides rapid, position-selectable initiation with minimal additional energy input that leaves neighboring cells undisturbed and is

therefore well suited to thermal propagation testing; lateral heating conforms to current standards such as GB 38031-2020 and represents the external-fire or failed-neighbor abuse scenario, at the cost of long preheating and a modified initial cell state.

Finally, the results provide cell-level reference data for the TR behavior of the emerging MCC chemistry: milder in peak temperature than high-nickel systems but still capable of sustained jet fires, with maximum measured temperatures of 682.6–775.4 °C at 100% SOC and venting-to-ignition delays of 9–20 s that define the window available for early warning and suppression. These data and the documented trigger dependence support trigger selection, comparability assessment, and the development of standardized TR and thermal propagation test protocols for manganese-based batteries.

Author Contributions: Conceptualization, C.J.; Methodology, C.J.; Validation, C.J., J.F., and H.L.; Formal analysis, C.J. and S.Z.; Investigation, C.J. and S.Z.; Resources, S.Z. and H.L.; Data curation, S.Z., J.F., and H.L.; Writing—original draft, C.J.; Writing—review & editing, C.X.; Visualization, S.Z., J.F., and H.L.; Supervision, J.F. and C.X.; Project administration, C.X.; Funding acquisition, C.X. All authors have read and agreed to the published version of the manuscript.

Funding: This research was funded by National Key R&D Program of China, grant number 2022YFB2404400.

Data Availability Statement: Dataset available on request from the authors.

Conflicts of Interest: The authors declare no competing interests.

References

1. Li, M.; Lu, J.; Chen, Z.; Amine, K. 30 years of lithium-ion batteries. *Adv. Mater.* **2018**, *30*, 1800561. [CrossRef] [PubMed]
2. Feng, X.; Ren, D.; He, X.; Ouyang, M. Mitigating thermal runaway of lithium-ion batteries. *Joule* **2020**, *4*, 743–770. [CrossRef]
3. Lai, X.; Yao, J.; Jin, C.; Feng, X.; Wang, H.; Xu, C.; Zheng, Y. A review of lithium-ion battery failure hazards: Test standards, accident analysis, and safety suggestions. *Batteries* **2022**, *8*, 248. [CrossRef]
4. Shen, K.; Sun, J.; Xu, C.; Wong, S.K.; Zheng, Y.; Jin, C.; Wang, H.; Chen, S.; Feng, X. Experimental Investigation for the Phase Change Material Barrier Area Effect on the Thermal Runaway Propagation Prevention of Cell-to-Pack Batteries. *Batteries* **2023**, *9*, 206. [CrossRef]
5. Jin, Y.; Meng, D.; Zhao, C.-X.; Yu, J.-L.; Wang, X.-H.; Wang, J. Experimental Study on Thermal Runaway Characteristics of High-Nickel Ternary Lithium-Ion Batteries under Normal and Low Pressures. *Batteries* **2024**, *10*, 287. [CrossRef]
6. Shi, C.; Wang, H.; Shen, H.; Wang, J.; Li, C.; Li, Y.; Xu, W.; Li, M. Thermal Runaway Characteristics and Gas Analysis of $LiNi_{0.9}Co_{0.05}Mn_{0.05}O_2$ Batteries. *Batteries* **2024**, *10*, 84. [CrossRef]
7. Wang, Z.; Li, L.; Heo, H.; Ren, L.; Wei, Y.; Lee, K.; Tian, H.; Xu, Z.; Sun, Z.; Kim, T.; et al. Synthesis and characterization of core–shell high-nickel cobalt-free layered $LiNi_{0.95}Mg_{0.02}Al_{0.03}O_2$@$Li_2ZrO_3$ cathode for high-performance lithium ion batteries. *J. Colloid Interface Sci.* **2024**, *666*, 424–433. [CrossRef] [PubMed]
8. Wang, S.; Zhang, C.; Chen, D.; Qin, Y.; Xu, L.; Li, Y.; Wang, Q.; Feng, X.; Wang, H. Explosion characteristics of two-phase ejecta from large-capacity lithium iron phosphate batteries. *eTransportation* **2024**, *22*, 100377. [CrossRef]
9. Wang, Q.; Wang, H.; Xu, C.; Jin, C.; Wang, S.; Xu, L.; Ouyang, J.; Feng, X. Multidimensional fire propagation of lithium-ion phosphate batteries for energy storage. *eTransportation* **2024**, *20*, 100328. [CrossRef]
10. Wang, R.; Liu, G.; Wang, C.; Ji, Z.; Yu, Q. A comparative study on mechanical-electrical-thermal characteristics and failure mechanism of LFP/NMC/LTO batteries under mechanical abuse. *eTransportation* **2024**, *22*, 100359. [CrossRef]
11. Zhang, X.; Yao, J.; Zhu, L.; Wu, J.; Wei, D.; Wang, Q.; Chen, H.; Li, K.; Gao, Z.; Xu, C.; et al. Experimental and simulation investigation of thermal runaway propagation in lithium-ion battery pack systems. *J. Energy Storage* **2024**, *77*, 109868. [CrossRef]
12. Jeong, S.Y.; Lee, S.; Lee, H.; Roh, K.-M.; Lee, C.-W.; Jeong, I.; Chae, M.S. Thermal characteristics of $LiMn_xFe_{1-x}PO_4$ (x = 0, 0.6) cathode materials for safe lithium-ion batteries. *J. Power Sources* **2025**, *626*, 235755. [CrossRef]
13. Guo, J.-X.; Gao, C.; Liu, H.; Jiang, F.; Liu, Z.; Wang, T.; Ma, Y.; Zhong, Y.; He, J.; Zhu, Z.; et al. Inherent thermal-responsive strategies for safe lithium batteries. *J. Energy Chem.* **2024**, *89*, 519–534. [CrossRef]
14. Wu, M.; Han, S.; Liu, S.; Zhao, J.; Xie, W. Fire-safe polymer electrolyte strategies for lithium batteries. *Energy Storage Mater.* **2024**, *66*, 103174. [CrossRef]
15. Shen, R.; Quan, Y.; McIntosh, J.D.; Salem, A.; Wang, Q. Fire safety of battery electric vehicles: Hazard identification, detection, and mitigation. *SAE Int. J. Electrified Veh.* **2024**, *13*, 279–294. [CrossRef]

16. Jin, C.; Sun, Y.; Wang, H.; Zheng, Y.; Wang, S.; Rui, X.; Xu, C.; Feng, X.; Wang, H.; Ouyang, M. Heating power and heating energy effect on the thermal runaway propagation characteristics of lithium-ion battery module: Experiments and modeling. *Appl. Energy* **2022**, *312*, 118760. [CrossRef]
17. *IEC 62619:2022*; Secondary Cells and Batteries Containing Alkaline or Other Non-Acid Electrolytes—Safety Requirements for Secondary Lithium Cells and Batteries, for Use in Industrial Applications. International Electrotechnical Commission: Geneva, Switzerland, 2022. Available online: https://webstore.iec.ch/publication/64073 (accessed on 15 August 2026).
18. *ANSI/CAN/UL 9540A*; Standard for Safety—Test Method for Evaluating Thermal Runaway Fire Propagation in Battery Energy Storage Systems. UL Standards & Engagement: Northbrook, IL, USA, 2019. Available online: https://www.shopulstandards.com/ProductDetail.aspx?UniqueKey=36503 (accessed on 15 August 2026).
19. *GB 38031-2020*; Electric Vehicles Traction Battery Safety Requirements. Standardization Administration of China: Beijing, China, 2020. Available online: http://www.gbstandards.org/GB_standard_english.asp?code=GB%2038031-2020 (accessed on 15 August 2026).
20. *SAE J2464-2021*; Electric and Hybrid Electric Vehicle Rechargeable Energy Storage System (RESS) Safety and Abuse Testing. SAE International: Warrendale, PA, USA, 2021. Available online: https://www.sae.org/standards/content/j2464_202108 (accessed on 15 August 2026).
21. *ISO 6469-1:2019/Amd 1:2022*; Electrically Propelled Road Vehicles—Safety Specifications—Part 1: Rechargeable Energy Storage System (RESS)—Amendment 1: Safety Management of Thermal Propagation. ISO: Geneva, Switzerland, 2022. Available online: https://www.iso.org/standard/73574.html (accessed on 15 August 2026).
22. Technical Report—Evaluation Tests for Thermal Propagation Resulting from Secondary Battery Thermal Runaway. 2021. Available online: https://www.test-navi.com/eng/report/pdf/EvaluationTestsForThermalPropagationResultingFromSecondaryBatteryThermalRunaway.pdf (accessed on 15 August 2026).
23. Jin, C.; Sun, Y.; Wang, H.; Lai, X.; Wang, S.; Chen, S.; Rui, X.; Zheng, Y.; Feng, X.; Wang, H.; et al. Model and experiments to investigate thermal runaway characterization of lithium-ion batteries induced by external heating method. *J. Power Sources* **2021**, *504*, 230065. [CrossRef]
24. Mulder, B.; Schöberl, J.; Birke, K.P. Thermal Propagation Test Bench with Multi Pouch Cell Setup for Reproducibility Investigations. *Batteries* **2023**, *9*, 447. [CrossRef]
25. Mei, J.; Shi, G.; Li, Q.; Liu, H.; Wang, Z. Experimental study on the effect of phase change material on thermal runaway characteristics of lithium-ion battery under different triggering methods. *J. Energy Storage* **2024**, *75*, 109832. [CrossRef]
26. Kriston, A.; Kersys, A.; Antonelli, A.; Ripplinger, S.; Holmstrom, S.; Trischler, S.; Döring, H.; Pfrang, A. Initiation of thermal runaway in Lithium-ion cells by inductive heating. *J. Power Sources* **2020**, *454*, 227914. [CrossRef]
27. Bayerl, T.; Duhovic, M.; Mitschang, P.; Bhattacharyya, D. The heating of polymer composites by electromagnetic induction—A review. *Compos. Part A Appl. Sci. Manuf.* **2014**, *57*, 27–40. [CrossRef]
28. Rudnev, V.; Loveless, D.; Cook, R.L. *Handbook of Induction Heating*; CRC Press: Boca Raton, FL, USA, 2017.
29. Lucia, O.; Maussion, P.; Dede, E.J.; Burdio, J.M. Induction heating technology and its applications: Past developments, current technology, and future challenges. *IEEE Trans. Ind. Electron.* **2013**, *61*, 2509–2520. [CrossRef]
30. Jin, C.; Sun, Y.; Zheng, Y.; Yao, J.; Wang, Y.; Lai, X.; Xu, C.; Wang, H.; Zhang, F.; Li, H.; et al. In situ observation of thermal runaway propagation in lithium-ion battery electrodes triggered by high-frequency induction heating. *Cell Rep. Phys. Sci.* **2023**, *4*, 101465. [CrossRef]
31. Jin, C.; Feng, X.; Sun, Y.; Wu, Z.; Zhang, F.; Lai, X.; Zheng, Y.; Xu, C.; Wang, H.; Yang, H.; et al. High-Frequency Induction Heating: A Breakthrough for Reliable Thermal Runaway Triggering in Battery Safety Testing. *ACS Energy Lett.* **2025**, *10*, 6054–6063. [CrossRef]
32. Huang, J.; Fan, Z.; Xu, C.; Jiang, F.; Feng, X. Experimental Investigation of Thermal Runaway Characteristics of Large-Format $Li(Ni_{0.8}Co_{0.1}Mn_{0.1})O_2$ Battery under Different Heating Powers and Areas. *Batteries* **2024**, *10*, 241. [CrossRef]
33. Shelke, A.V.; Buston, J.E.; Gill, J.; Howard, D.; Williams, R.C.; Read, E.; Abaza, A.; Cooper, B.; Richards, P.; Wen, J.X. Combined numerical and experimental studies of 21700 lithium-ion battery thermal runaway induced by different thermal abuse. *Int. J. Heat Mass Transf.* **2022**, *194*, 123099. [CrossRef]
34. Liu, Y.; Zhang, L.; Ding, Y.; Huang, X.; Huang, X. Effect of thermal impact on the onset and propagation of thermal runaway over cylindrical Li-ion batteries. *Renew. Energy* **2024**, *222*, 119910. [CrossRef]
35. Mahdy, O.S.; Ali, A.B.M.; Mostafa, L.; Agarwal, D.; Dhawan, A.; Mabrouk, A.; Kolsi, L.; Ben Said, L. Quantitative evaluation of thermal runaway in lithium-ion batteries under critical heating conditions to enhance safety. *Sci. Rep.* **2025**, *15*, 24004. [CrossRef] [PubMed]
36. Shen, H.; Wang, H.; Li, M.; Li, C.; Zhang, Y.; Li, Y.; Yang, X.; Feng, X.; Ouyang, M. Thermal Runaway Characteristics and Gas Composition Analysis of Lithium-Ion Batteries with Different LFP and NCM Cathode Materials under Inert Atmosphere. *Electronics* **2023**, *12*, 1603. [CrossRef]

37. Song, L.; Huang, Z.; Mei, W.; Jia, Z.; Yu, Y.; Wang, Q.; Jin, K. Thermal runaway propagation behavior and energy flow distribution analysis of 280 Ah $LiFePO_4$ battery. *Process Saf. Environ. Prot.* **2023**, *170*, 1066–1078. [CrossRef]
38. Mao, B.; Liu, C.; Yang, K.; Li, S.; Liu, P.; Zhang, M.; Meng, X.; Gao, F.; Duan, Q.; Wang, Q.; et al. Thermal runaway and fire behaviors of a 300 Ah lithium ion battery with $LiFePO_4$ as cathode. *Renew. Sustain. Energy Rev.* **2021**, *139*, 110717. [CrossRef]

Disclaimer/Publisher's Note: The statements, opinions and data contained in all publications are solely those of the individual author(s) and contributor(s) and not of MDPI and/or the editor(s). MDPI and/or the editor(s) disclaim responsibility for any injury to people or property resulting from any ideas, methods, instructions or products referred to in the content.